

# Surrogate based high-fidelity rapid design optimization of rotor blades used in a small unmanned aerial vehicle

Jiarui Hao<sup>1</sup> (M.Eng. Candidate), Liye Lv<sup>2\*</sup> (PhD. Candidate), Xiaobang Wang<sup>3</sup> (PhD. Candidate), Xueguan Song (Professor, PhD)

<sup>1</sup> School of Mechanical Engineering, Dalian University of Technology, No. 2 Linggong Road, Ganjingzi District, Dalian 116024, China e-mail: hjr@mail.dlut.edu.cn

<sup>2</sup> School of Mechanical Engineering, Dalian University of Technology, No. 2 Linggong Road, Ganjingzi District, Dalian 116024, China e-mail: lvhexiaoye@mail.dlut.edu.cn

<sup>3</sup> School of Mechanical Engineering, Dalian University of Technology, No. 2 Linggong Road, Ganjingzi District, Dalian 116024, China e-mail: wxbang@mail.dlut.edu.cn

\* School of Mechanical Engineering, Dalian University of Technology, No. 2 Linggong Road, Ganjingzi District, Dalian 116024, China e-mail: sxg@dlut.edu.cn

## Abstract:

Due to the complicated geometry of the Unmanned Aerial Vehicle (UAV) rotor and the high sensitivity of the aerodynamic performance to the blade shape, many deficiencies exist in the current design and optimization of three-dimension (3D) rotor blades, such as dimensionality curses and large computational costs. To address these problem, a new optimization framework with a high-fidelity model is developed. The high-accuracy CFD model is built with rotor thrust errors within 4.8% compared with experimental data. A 3D blade model based on the Class Function/shape Function Transformation (CST) method is proposed. Four surrogate models are

constructed for rotor thrust and torque and the Kriging (KRG) model with the highest precision is selected. Genetic Algorithm (GA) is used to perform the optimization of the torque at hovering thrust level. Compared with the E387 baseline rotor, optimization results show that the torque and the mass reduce by 10.71% and 26.78%, respectively, and the Figure of Merit (FM) increases by 4.5%. Then, the one-way fluid-structural interaction are carried out to verify the feasibility of the proposed optimization framework.

**Keywords:**

CFD, fluid-structural interaction, high-fidelity rapid optimization, surrogate model, Unmanned Aerial Vehicle

## **1. Introduction**

Since Unmanned Aerial Vehicle (UAV) is now widely used in the agriculture, the mapping and the transportation, it is greatly significant to perform a high-fidelity design optimization for the rotor blade to improve the endurance and the load capacity. Currently, Computational Fluid Dynamics (CFD ) is the most widely used technique to make an intuitive description of the flow field while ensuring high accurate solutions, due to which it has also been applied in the blade analysis and design. Yun (Yun 2014) performed the CFD simulations of UAV in hover state to explore the effect of blade shape to the thrust performance, results show that the arc edge produces more thrust. Sugiura (Sugiura, Tanabe, Sugawara, etc. 2014) used the Genetic Algorithm (GA) to determine the optimal distribution of the chord length and the twist angle for a UAV blade.

Benaouali (Benaouali and Kachel 2017) carried out the Sequential Quadratic Programing (SQP) algorithm to optimize the subsonic wing planform parameters. From all the work above, few section parameters coupled with planform parameters are optimized in these work because of the limitation of blade parameterization model. Garg (Garg, Kenway, Martins, etc. 2017) used the Free Format Deformation (FFD) (Sederberg and Parry 1986) method coupled with CFD simulation to optimize the hydrofoil shape by taking into account 210 parameters. Kenway (Kenway and Martins 2016) also parameterized the Common Research Model (CMR) fixed-wing with 768 FFD parameters and performed the simulation-driven optimization to search the efficiency shape. However, the full geometric description and high-fidelity CFD model were performed in both two researches, the optimization framework is not suitable for UVA rotor blade because of its expensive computation caused by the big number of variables.

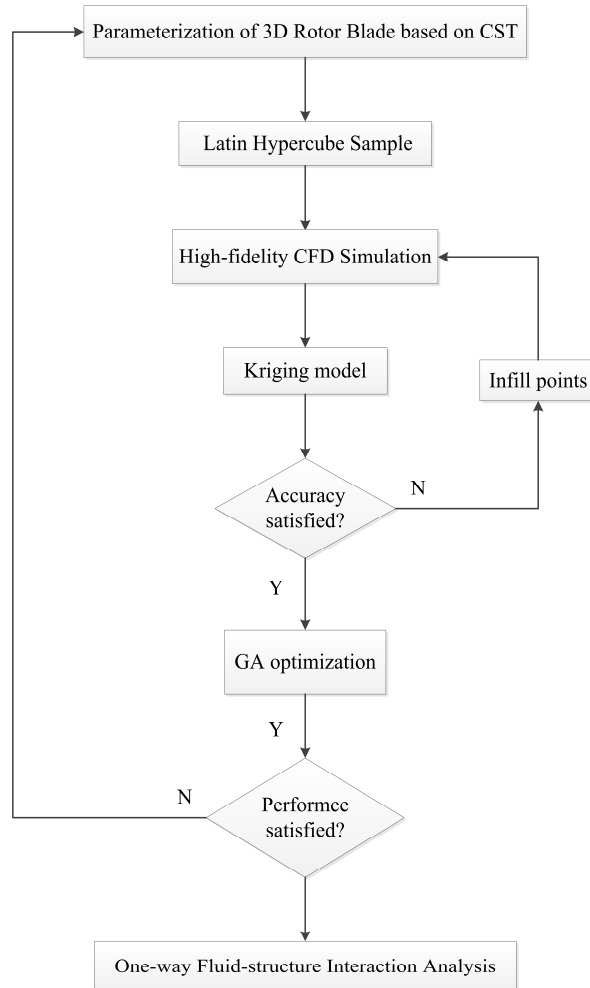
To address the problems mentioned above, the Class Function/Shape Function Transformation (Kulfan 2008) (CST) airfoil parameters and planform parameters are both used to describe the 3D blade geometry in this paper. The model is simplified for the small UAV, but the airfoil changes in radial direction are guaranteed. To further decrease the computational burden, a surrogate model built using the CFD data is used in optimization process. There are four typical surrogate models, namely the polynomial response surface (PRS) (Myers and Montgomery 1995), the radial basis function (RBF) (Gutmann 2001, Sun 2011), the Kriging (KRG) (Matheron 1963, Sacks 1989), and the support vector regression (SVR) (Smola 2004). As the mathematical approximation method which can formulate the relationship between objectives/constraints and design variables, surrogate model has been widely used in design of the aircraft and the wind turbine. Lee (Lee, Ryu, Ahn and

Kwon 2014) conducted the CFD-based genetic algorithm coupled with the Kriging model to optimize the distribution of the twist angle and the chord length for a UAV in hover state and made the blade more efficient in off-design conditions. Wang (Wang, Li, Zhang, etc. 2015) performed the lightweight design for the Composite Wind Turbine Blade based on RBF model. Badhurshah (Badhurshah and Samad 2015) established a high-fidelity multiple surrogate model based on PRS, RBF, KRG, and Weighted average surrogates (WAS) to optimize a bi-directional impulse turbine.

In this paper, the rapid optimization framework which guarantee its high-fidelity model in design process for rotor blades of a small UAV is established. Firstly, the researchers build up the high-fidelity CFD model of rotor with errors within 4.8% all over the operating conditions. Then, the blade shape is parameterized based on CST method with 22 parameters and the Latin Hypercube Sample (LHS) (Shields, Zhang 2016) is used to perform the design of experiment (DoE) which are employed to construct the surrogate model of the rotor blades. The Generic Algorithm is utilized to optimize the torque at hovering thrust level which is subject to the airfoil thickness and the twist angle.

This paper is organized as follows. The methodologies are explained in Section 2, followed by parameterization of the baseline model and the experiment validation of its CFD model in Section 3. Section 4 constructs different surrogate models among which with the model with the highest accuracy is selected. Section 5 describes the optimization formulation of the blade optimization. The optimal results and its validation in off-design conditions are given in Section 6 compared with the baseline results. Section 7 performs the one-way fluid-structural interaction to confirm the structural safety. Finally, our findings are summarized in Section 8. The flow chart of design

85 and optimization framework is shown in Fig 1.



86  
87 **Fig. 1.** Design and optimization framework of rotor blades

88

89 **2. Methodology**

90 **2.1 CFD solver**

91 The air flow is governed by 3-D compressible Reynolds Average Navier Stokes (RANS)

92 equations:

$$\begin{cases} \frac{\partial \rho_f}{\partial t} + \frac{\partial}{\partial x_j} [\rho_f v_j] = 0 \\ \frac{\partial \rho_f v_i}{\partial t} + \frac{\partial}{\partial x_j} [\rho_f v_i v_j + p \delta_{ij} - \tau_{ij}] = 0, i, j = 1, 2, 3 \\ \frac{\partial E}{\partial t} + \frac{\partial}{\partial x_j} [E v_j + p v_j + q_j - v_i \tau_{ij}] = 0 \end{cases} \quad (1)$$

where the subscript indices  $i, j$  stand for directions of  $x, y, z$ , respectively;  $\rho_f$  is the fluid density;  $v$  is the flow velocity flow;  $p$  is the fluid pressure;  $\tau$  represents the fluid shear stress tensor;  $E$  is the flow energy;  $q$  is the heat flux vector of the fluid and  $\delta_{ij}$  is the Kronecker delta.

## 2.2 Class Function/shape Function Transformation method

The Class Function/shape Function Transformation method is a parametric method proposed by Kulfan to describe the geometry of airfoils with high accuracy and continuous smooth geometric curves (Sripawadkul, Padulo and Guenov 2010). This parametric function can be expressed with two parts: class function and shape function:

$$\begin{cases} \zeta_U(\psi) = C_{N_2}^{N_1}(\psi) S_U(\psi) + \psi \cdot \Delta \zeta_U \\ \zeta_L(\psi) = C_{N_2}^{N_1}(\psi) S_L(\psi) + \psi \cdot \Delta \zeta_L \\ \psi = x / c \\ \zeta = z / c \end{cases} \quad (2)$$

where  $c$  represents the chord length;  $x$  and  $z$  are the coordinates of points on airfoil curve along the chord length and its vertical direction, respectively;  $\psi$  and  $\zeta$  are the non-dimensional expression of  $x$  and  $z$ ;  $\zeta_U$  and  $\zeta_L$  represent the normalized coordinates of upper and lower airfoil curve, respectively;  $\psi \cdot \Delta \zeta_U$  and  $\psi \cdot \Delta \zeta_L$  define the thickness of trailing edge, respectively.

107 Class function  $C_{N_2}^{N_1}(\psi)$  can be written as Eq. (3):

$$108 \quad C_{N_2}^{N_1}(\psi) = \psi^{N_1} \cdot (1 - \psi)^{N_2} \quad (3)$$

109 where values of  $N_1$  and  $N_2$  are determined by the characteristics of the airfoil leading edge,  
110 which are set to be 0.5 and 1 in this paper, respectively.

111 Shape functions  $S_U(\psi)$  and  $S_L(\psi)$  are written as Eq. (4)

$$112 \quad \begin{cases} S_U(\psi) = \sum_{i=0}^{N_U} A_U(i) \cdot S(\psi, i) \\ S_L(\psi) = \sum_{i=0}^{N_L} A_L(i) \cdot S(\psi, i) \end{cases} \quad (4)$$

113 where  $S$  is the Bemstein polynomial;  $N_U$  and  $N_L$  are orders of Bemstein polynomial for upper  
114 and lower airfoil curve, respectively;  $A_U$  and  $A_L$  are the corresponding coefficients. The N-order  
115 Bemstein polynomial is defined as Eq. (5)

$$116 \quad \begin{cases} S(\psi, i) = K_i^N \cdot \psi^i \cdot (1 - \psi)^{N-i} \\ K_i^n = \frac{n!}{i!(n-i)!} \end{cases} \quad (5)$$

117 In summary, the control polynomial of upper and lower airfoil curve can be written as Eq. (6)

$$118 \quad \begin{cases} \zeta_U(\psi) = \psi^{0.5} \cdot (1 - \psi)^{1.0} \sum_{i=0}^{N_U} [A_U(i) \cdot \frac{N_U!}{i!(N_U-i)!} \cdot \psi^i \cdot (1 - \psi)^{N_U-i}] + \psi \cdot \Delta \zeta_U \\ \zeta_L(\psi) = \psi^{0.5} \cdot (1 - \psi)^{1.0} \sum_{i=0}^{N_L} [A_L(i) \cdot \frac{N_L!}{i!(N_L-i)!} \cdot \psi^i \cdot (1 - \psi)^{N_L-i}] + \psi \cdot \Delta \zeta_L \end{cases} \quad (6)$$

119 Therefore, the 2-D airfoil geometry can be represented by CST function easily if the correct  
120 Bemstein polynomial coefficients ( $A_U$  and  $A_L$ ) are determined. On the other hand, the  
121 polynomial coefficients can also be design variables for airfoil aerodynamic optimization.

122

123

### 3. Baseline blade model

All of the optimization results in this paper are based on the E387 airfoil rotor blade with the material being Polycarbonate. The operating parameters are shown in Table 1. The material properties are shown in Table 2. The rotor and its 3-D model are shown in Fig. 2 (a) and (b), respectively.

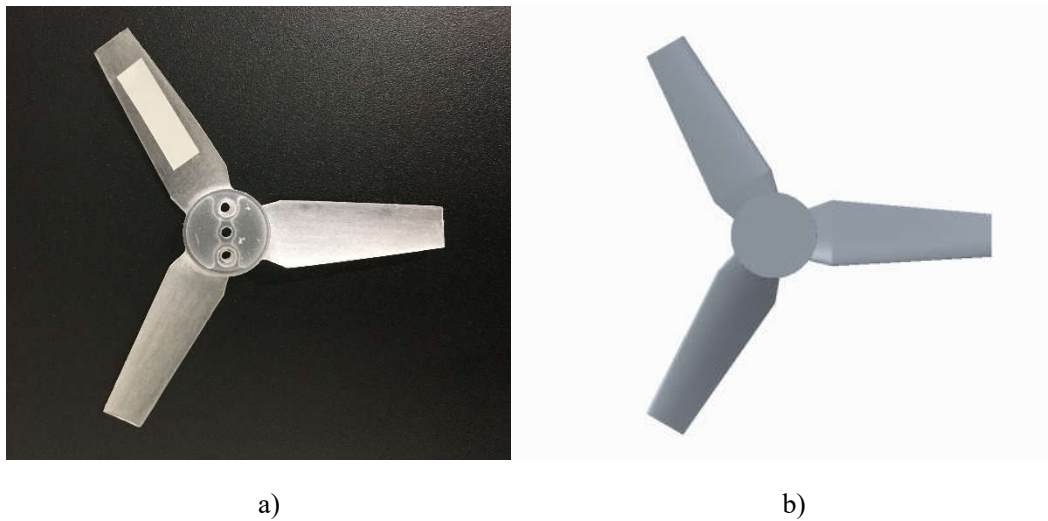


**Fig. 2.** Baseline rotor and 3-D model

#### 3.1 Parametric modeling

Due to the complexity of the rotor blade geometry, the parametric modeling of blade shape can be divided into two parts. The first part is the description of planform, including the chord length, twist angle distribution, forward sweep or back sweep, tip ratio, etc. The other part is the parametric modeling of airfoil section, including several geometric modeling methods such as Ferguson's curves (Ferguson 1964), Hicks-Henne bump functions (Hicks, Henne 1978), Parametric Section (PARSEC) (Ray and Tsai 2004, Sobieczky 1998), Class Function/shape Function Transformation (CST), and so on. Considering the orthogonality, flawlessness and intuitiveness of



the airfoil parametric model, the 3rd-order CST function parameters are combined with planform parameters to represent the UAV blade 3-D geometry, of which 22 variables are used for rapid optimization.

**Fig. 3.** Planform parameters

Figure 3 shows the geometric meaning of the planform parameters. The radius of rotor  $R$  is fixed at 45 mm. Geometries of the planform and airfoil are depended on how to set the parameters of the tip section and maximum-chord section (called middle section in this paper). As shown in Fig. 3, the root section is fixed. The position of middle section is represented by  $d_{mt}$ .  $O$  is the twist center of 2-D airfoil section which is located by the normalized value  $\varepsilon$ . When  $\varepsilon = 0$ ,  $O$  is at leading edge of airfoil and the swept forward is equal to 0. Table 3 shows the baseline parameters of the planform.

For the description of the baseline airfoil (E387), the 3rd-order CST parameterization method is adopted. The geometric error is minimized by the *fmincon* function built-in the *Matlab* optimization toolbox, and the CST parameters of the upper and lower airfoil surfaces are determined. The E387 model and the corresponding CST fitting model are shown in Fig. 4. The 3rd-order CST parameters and errors are shown in Table 4.

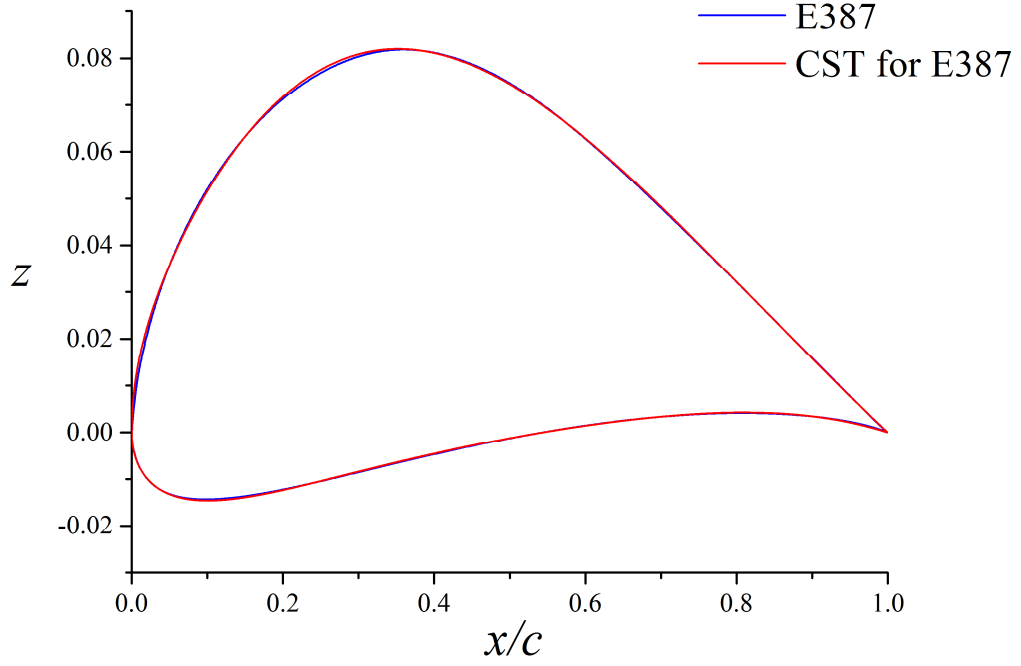


**Fig. 4.** Comparison between E387 airfoil and its CST fitting result

### 3.2 Fluid model validation

The commercial software ANSYS ICEM and ANSYS CFX are used for dividing grids and CFD simulations. Due to the different complex geometric shapes of the training set samples, dividing the structural grid faces a tremendous amount of work. To reduce generation time of grid, a hybrid grid is employed in this paper. Two types of grids are used to mesh the flow field, unstructured grids for the inner domain and structured grids for the outer domain. The amount of baseline grid nodes is 1,041,171. Figure 5 shows the flow field grid (a) and the detail of boundary layers (b). Table 5 presents the mesh information.

a) b)

**Fig. 5.** CFD mesh for the baseline blade

**Fig. 6.** Boundary conditions of the computational domain in ANSYS CFX

Figure 6 shows the boundary conditions of the flow field in ANSYS CFX. The top, bottom and the cylindrical surface of outer domain are set to open; the sides are the interfaces, and the rotational periodicity conditions are set according to the rotation speed of the rotor. The hub and the blade surfaces are set as walls. The Shear Stress Transport (SST) turbulence model (Menter, 2009) is applied in the simulations.

**Fig. 7.** Schematic diagram of experimental device for measuring rotation speed and rotor thrust

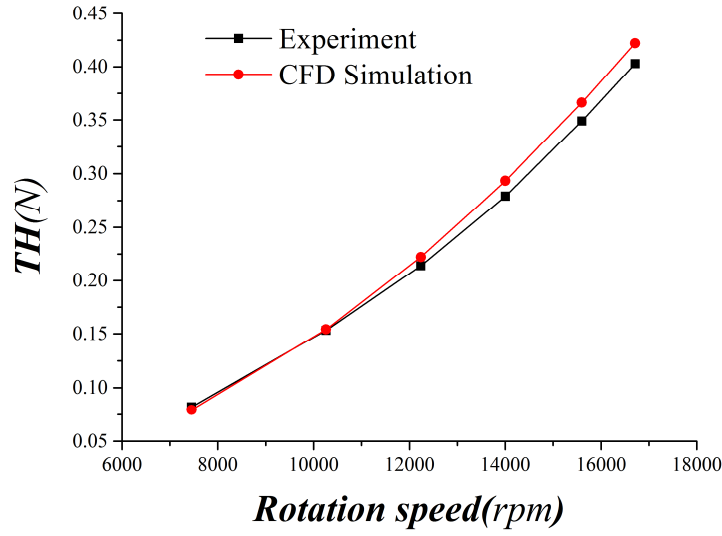


**Fig. 8.** Comparison of rotor thrust between CFD results and experimental data

CFD solutions are compared to the experimental measurements over the operating conditions. The high-fidelity fluid model with errors within 4.8% on rotor thrust over all the rotation speed is validated. The schematic diagram of experimental device is shown in Fig. 7. Pulse-Width Modulation (PWM) is used for the step speed regulation of the motor and high-precision electronic scale is applied to thrust measurement. The rotation speed is measured by the laser velocimeter. Fig. 8 shows the comparison of rotor thrust between CFD results and experimental data.

#### 4. Surrogate model construction

As the low Reynolds operating conditions of the small UAV rotor, the boundary of the airfoil parameters is determined with reference to other low Reynolds number airfoils which have been analyzed before (Drela and Gilest 1987, Selig and Guglielmo 1997, Singha, Ahmeda and Zullahb

2012) such as REA2822, SG6043, FX 63-137, etc. The boundaries of all 22 design variables are listed in Table 6. 6 random samples in airfoil design space and the baseline airfoil are shown in Fig. 9.

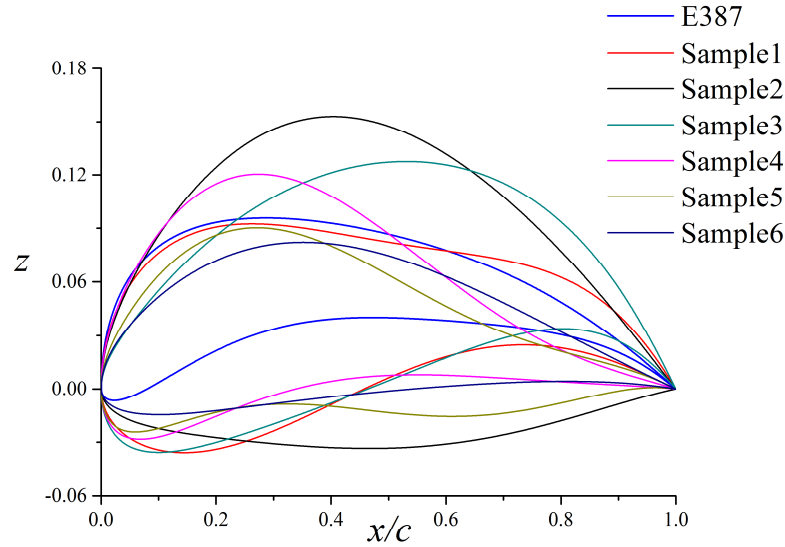
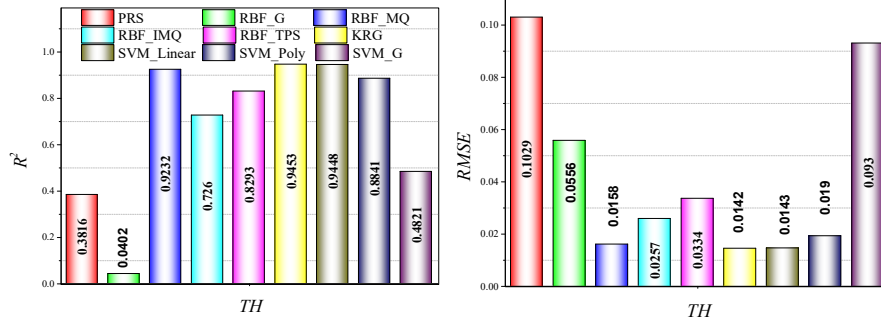
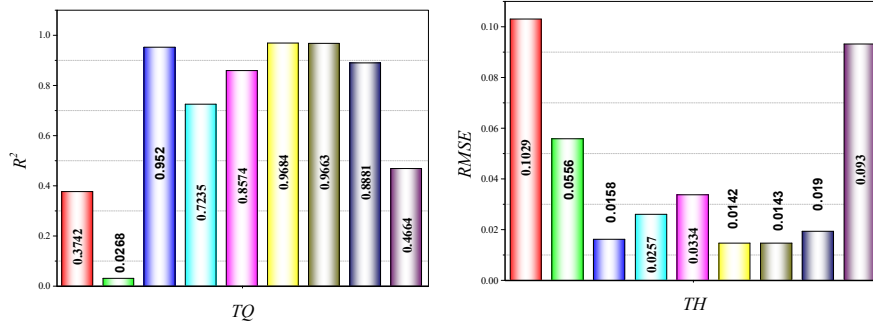


**Fig. 9.** Airfoil samples for 3-order CST parameterization

Based on the thrust and torque data of the Latin Hypercube Sample models containing 220 training points different surrogate models (PRS, KRG, RBF and SVR) are constructed, inclusive of different basis function for RBF and SVR. To assess the accuracies of surrogate models, two criteria, namely root mean square error ( $RSME$ ) and coefficient of determination ( $R^2$ ) are used based on the extra 50 testing points. The comparison of these surrogate models for  $TH$  and  $TQ$  are shown in Fig.10 (a) and (b), respectively. The KRG models for both  $TH$  and  $TQ$  with highest  $R^2$  and lowest  $RSME$  are selected to use for rapid optimization.



a)



b)

**Fig. 10.** Comparison of the surrogate models on  $R^2$  and  $RMSE$

## 5. High fidelity optimization establishment

To improve the efficiency and endurance of the UAV rotor, the design optimization problem is to minimize the rotor torque by changing the blade geometry at the baseline hovering rotation speed (12000rpm). The rotor thrust is constrained to be equal to the thrust at baseline hover state. The negative twist is set up to save the search time for efficiency blade (Yun, Choi and Lee 2014). The CST parametric constraint and thickness constraint are considered to guarantee the availability of the result. GA algorithm built-in *Matlab toolbox* is applied to search the optimal solution. The optimization formulation problem is shown in Table 7.

## 6. Results

After 100 iterations, the optimal results can be obtained. The iterative histories of objective function ( $TQ$ ) and constraint function ( $TH$ ) are shown in Fig. 11. The optimal parameters are shown in Table 8.

**Fig. 11.** Optimization history of  $TH$  and  $TQ$

a)

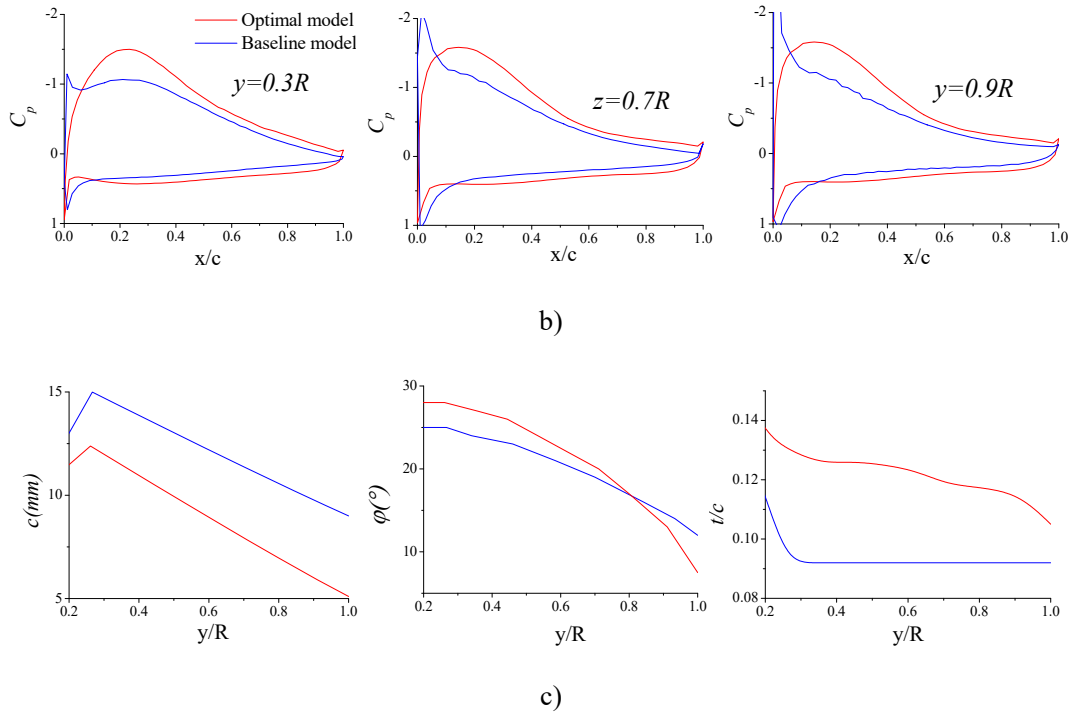


**Fig .12.** Comparison between the optimized rotor blade and the E387 baseline

Figure 12 compares the CFD simulation results of optimized rotor blade to the E387 baseline. The optimized blade yields a 10.71% reduction in torque, a 4.5% increase in FM and a 26.78% reduction in mass relative to E387 baseline. Figure 12(a) shows the  $C_p$  contour of baseline blade and optimization blade on both suction side and pressure side. Apparently, the pressure nearby the trailing edge of optimized blade is relatively flat and the proportion of low pressure area on blade surface is much higher. Figure 12(b) shows the geometry profiles and the  $C_p$  distribution at three spanwise sections ( $y=0.3 R$ ,  $0.7 R$ , and  $0.9 R$ ). The radial distribution of airfoil chord length, twist angle, and thickness of the two model are shown in Figure 12(c). Compared to the baseline blade, the negative twist gradient of optimized model and the curvature of its airfoil camber is larger than



the E387 baseline. The chord length becomes shorter and the airfoil thickness is increased.

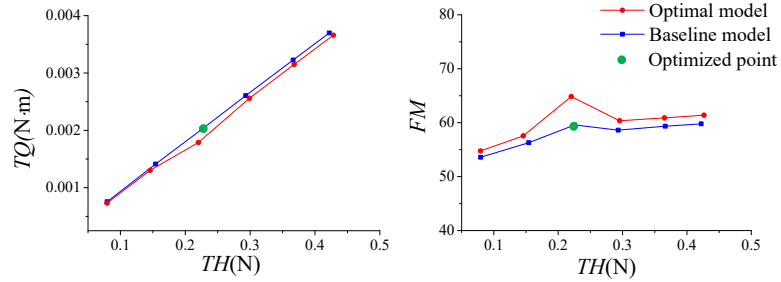


**Fig. 13.** Aerodynamic performance of optimized rotor in off-design conditions

To check the aerodynamic performance of optimized blade at other off-design conditions, the CFD simulations all over the working speed have been conducted. As shown in Fig. 13, the lower torque TQ and the higher FM of optimized blade is guaranteed at the other operating state. The efficiency of the optimized blade is ensured.

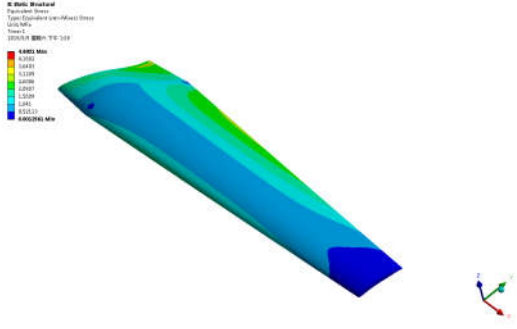
## 7. Fluid-structural Interaction Analysis

To assure the safety factor of the optimized blade, the one-way fluid-structure interaction (FSI) is carried out at the limit state (16500 rpm). The high-fidelity structural analysis using FEM method and the high-fidelity CFD simulations are combined to calculate the stress and strain.

**Fig. 14.** Loads on UAV rotor blade (Kwon, Yi and Choi 2015)

The commercial software *ANSYS workbench* is applied for grid generation and static structural analysis. The grid is shown in Fig. 14. As shown in Table 9, the structural safety factor of optimized model is equal to 11.75 which is larger than 6.68 presented the safety factor of baseline model, therefore the safety of structure is ensured. The stress and deformation distribution of baseline blade and optimized blade is shown in Fig 15.

a) Baseline blade



b) Optimized blade

**Fig. 15.** Equivalent stress distribution (left) and total deformation distribution (right)

## 8. Conclusions & Future work

For computational efficiency of UAV rotor blade optimization, a rapid high-fidelity design framework based on surrogate model is proposed in this paper. Based on the CST method, the 3-D geometry model of the blade is parameterized with only 22 variables containing 6 planform parameters and 16 section parameters. 220 training points and 50 testing points were randomly generated using LHS method, and the corresponding outputs are obtained by substituting the samples into the high-fidelity CFD simulations. Based on the samples, four surrogate models (PRS, RBF, SVR, and Kriging) were constructed and the KRG model was the best one. GA algorithm coupled with the selected KRG model was performed to minimize the torque at hovering thrust level subject to the airfoil thickness and twist angle constraints. The optimized model showed a larger negative twist which was  $25^\circ$  (mid) to  $12^\circ$  (tip) originally but  $27.79^\circ$  to  $7.54^\circ$  now. Meanwhile, the curvature of airfoil camber and the airfoil thickness is larger than the E387 baseline. The pressure nearby the trailing edge is relatively flat and the proportion of low

pressure area is higher, which could make it more productive on thrust without increasing the area of the blade.

The optimized blade yielded a 10.71% reduction in torque, a 4.5% increase in FM and a 26.78% reduction in mass relative to E387 baseline. Finally, the good performance under off-design conditions and the structural safety of optimized blade were ensured. Compared with the geometry of the baseline blade, it could be concluded that an appropriate increase in the airfoil camber, the negative twist of the blade and the airfoil thickness can improve the efficiency of the small UAV rotor working under the low Reynolds number. The validity of the proposed rapid design optimization framework is ensured. To improve the rotor efficiency all over the UAV operating conditions, the multipoint optimization framework considering both forward flight and hover state will be conducted in the future.

## Notation

*The following symbols are used in this paper:*

$c$	Chord length (mm);
$C_p$	Pressure coefficient, $C_p = \frac{P_{local} - P_{ref}}{0.5\rho_f V^2}$ ;
$C_T$	Thrust coefficient, $C_T = \frac{TH}{0.5\rho \cdot \pi \cdot \Omega^2 R^4}$ ;
$C_Q$	Torque coefficient, $C_Q = \frac{TQ}{0.5\rho \cdot \pi \cdot \Omega^3 R^5}$ ;
$E_s$	Young modulus (Gpa);
$FM$	Figure of merit (efficiency), $FM = \frac{C_T^{1.5}}{2C_Q}$ ;

$P_{local}$	Local fluid pressure (Pa);
$P_{ref}$	Reference upstream pressure (Pa);
$R$	Radius of rotor (mm);
$Re$	Reynolds number;
$t$	Airfoil thickness (mm);
$TH$	Rotor Thrust (N);
$TQ$	Rotor Torque (N·m);
$V$	Inflow velocity (m/s);
$\varphi$	Twist angle (°);
$\rho_s$	Solid density (kg/m <sup>3</sup> );
$\rho_f$	Fluid density (kg/m <sup>3</sup> );
$\nu_s$	Poisson's ratio;
$\sigma_y$	Yield strength (Mpa);
$\Omega$	Potation speed of rotor (rad/s).

307

308

## References

- Benaouali Abdelkader and Kachel Stanisław. (2017) "A surrogate-based integrated framework for the aerodynamic design optimization of a subsonic wing planform shape." *Proceedings of the Institution of Mechanical Engineers, Part G: Journal of Aerospace Engineering*, 232(5), 872-883
- Badhurshah Rameez and Samad Abdus. (2015) "Multiple surrogate based optimization of a bidirectional impulse turbine for wave energy conversion." *Renewable Energy*, 74, 749-760.
- Drela Mark and Gilest M. B (1987) "Viscous-inviscid analysis of transonic and low reynolds number airfoils." *AIAA Journal*, 25(10), 1347-1355
- Ferguson James (1964) "Multivariable curve interpolation." *Journal of the Association for Computing Machinery*, 11(2), 221-228
- Gutmann H. M (2001) "A radial basis function method for global optimization." *Journal of Global Optimization*, 19(3), 201-227.
- Garg Nitin, Kenway Gaetan K.W, Martins Joaquim R.R.A., etc. (2017) "High-fidelity multipoint hydrostructural optimization of a 3-D hydrofoil." *Journal of Fluids and Structures*, 71, 15-39
- Hicks, R. and Henne, P. (1978) "Wing Design by Numerical Optimization." *Journal of Aircraft*, 15(7), 407-413

331 Kwon Hyung-Il, Yi Seulgi, Choi Seongim, etc. (2015) "Design of efficient propellers using variable-fidelity  
332 aerodynamic analysis and multilevel optimization." *Journal of Propulsion and Power*, 31(4), 1057-1073  
333  
334 Kenway Gaetan K. W and Martins Joaquim R. R. A. (2016) "Multipoint aerodynamic shape optimization  
335 investigations of the common research model wing." *AIAA Journal*, 54(1), 113-128  
336  
337 Kulfan Brenda M (2008) "Universal parametric geometry representation method." *Journal of Aircraft*, 45(1),  
338 142-158.  
339  
340 Lee H.M, Ryu J.K, Ahn S.J and Kwon O.J (2014) "Aerodynamic design optimization of UVA rotor blades using a  
341 Genetic algorithm and Artificial Neural Networks." *Journal of Computational Fluids Engineering*, 19(3), 29-36  
342  
343 Menter F. R (2009) "Review of the SST turbulence model experience from an industrial perspective." *International*  
344 *Journal of Computational Fluid Dynamics*, 23(4), 305-316.  
345  
346 Matheron G (1963) "Principles of geostatistics." *Economic geology*, 58(8), 1246-1266.  
347  
348 Myers R. H and Montgomery D.C (1995) *Response surface methodology: process and product in optimization using*  
349 *designed experiments*. U.S  
350  
351 Ray T and Tsai H. M (2004) "Swarm algorithm for single- and multiobjective airfoil design optimization." *AIAA*  
352 *Journal*, 42(2), 336-673

353

354 Shields Michael D and Zhang Jiaxin (2016) “The generalization of Latin hypercube sampling.” *Reliability*  
355 *Engineering and System Safety*, 148, 96-108.

356

357 Sobieczky, H. (1998) “Parametric Airfoils and Wings.” *Notes on Numerical Fluid Mechanics*, 16, 71-88

358

359 Singha Ronit K, Ahmeda M. Rafiuddin, Zullahb Mohammad Asid, etc. (2012) “Design of a low reynolds number  
360 airfoil for small horizontal axis wind turbines.” *Renewable Energy*, 42(1), 66-76

361

362 Sugiura Masahiko, Tanabe Yasutada, Sugawara Hideaki, etc. (2014) “Computationally efficient and high fidelity  
363 optimization of rotor blade geometry.” *40th European Rotorcraft Forum*, 2014, 2, 1389-1394

364

365 Selig Michael S and Guglielmo James J (1997) “High-lift low reynolds number airfoil design.” *Journal of aircraft*,  
366 34(1), 72-79

367

368 Sripawadkul V, Padulo M and Guenov M (2010) “A Comparison of airfoil shape parameterization techniques for  
369 early design optimization.” *13th AIAA/ISSMO Multidisciplinary Analysis Optimization Conference*, American

370 Institute of Aeronautics and Astronautics

371

372 Sacks J, Welch W. J, Mitchell T. J and Wynn H. P (1989) “Design and analysis of computer experiments.”  
373 *Statistical Science*, 4(4), 409–435.

374



375 Sederberg Thomas W and Parry Scott R (1986) "Free-form deformation of solid geometric models." *ACM*  
376 *SIGGRAPH Computer Graphics*, 20(4), 151-160  
377  
378 Sun G Y, Li G Y, Gong Z H, He G Q and Li Q. (2011) "Radial basis functional model for multiobjective sheet  
379 metal forming optimization." *Engineering Optimization*, 12(43), 1351-1366.  
380  
381 Smola A J and Schölkopf B. (2004) *A tutorial on support vector regression*. Kluwer Academic Publishers. The  
382 Kingdom of Netherlands  
383  
384 Wang Yongzhi, Li Feng and Zhang Xu, etc. (2015) "Composite wind Turbine blade aerodynamic and structural  
385 integrated design optimization based on RBF meta-model." *Materials Science Forum*, 813, 10-18  
386  
387 Yun Jae Hyun, Choi Ha-Young and Lee Jongsoo (2014). "CFD-based thrust analysis of unmanned aerial vehicle  
388 in hover mode: effects of single rotor blade shape." *Transactions of the Korean Society of Mechanical Engineers A*,  
389 38(5), 513-520.

390 **Fig. 1.** Design and optimization framework of rotor blades

391 **Fig. 2.** Baseline rotor and 3-D model

392 **Fig. 3.** Planform parameters

393 **Fig. 4.** Comparison between E387 airfoil and its CST fitting result

394 **Fig. 5.** CFD mesh for the baseline blade

395 **Fig. 6.** Boundary conditions of the computational domain in ANSYS CFX

396 **Fig. 7.** Schematic diagram of experimental device for measuring rotation speed and rotor thrust

397 **Fig. 8.** Comparison of rotor thrust between CFD results and experimental data

398 **Fig. 9.** Airfoil samples for 3-order CST parameterization

399 **Fig. 10.** Comparison of the surrogate models on  $R^2$  and  $RMSE$

400 **Fig. 11.** Optimization history of  $TH$  and  $TQ$

401 **Fig. 12.** Comparison between the optimized rotor blade and the E387 baseline

402 **Fig. 13.** Aerodynamic performance of optimized rotor in off-design conditions

403 **Fig. 14.** Loads on UAV rotor blade (Kwon, Yi and Choi 2015)

404 **Fig. 15.** Equivalent stress distribution (left) and total deformation distribution (right)

405

406

**Table 1.** Parameters of UAV operating

<i>Cross section</i>	<i>E387</i>
Working speed	5000~17000rpm
Re	$2 \sim 6 \times 10^4$
Hovering speed	12000rpm
Fluid	Air
Material	Polycarbonate
$T_f$	25°C

407

408

**Table 2.** Polycarbonate properties material

Symbol	Description	Value	Units
$\rho_s$	Solid density	1200	$\text{kg}(m^3)$
$E_s$	Young modulus	2.3~2.4	Gpa
$\nu_s$	Poisson's ratio	0.37	-
$\sigma_y$	Yield strength	55~75	Mpa

409

410

411

412

413

414 **Table 3.** Values of the baseline planform parameters

Planform parameters	Baseline Value
$\varphi_{tip} (^{\circ})$	12
$\varphi_{mid} (^{\circ})$	25
$c_{tip} (\text{mm})$	9
$c_{mid} (\text{mm})$	15
$d_{mt} (\text{mm})$	33
$\varepsilon$	0.4

415

416 **Table 4.** Values of E387 CST parameters

E387	CST parameters	Value
	$A_{U0}$	-0.0678
	$A_{U1}$	0.00554
	$A_{U2}$	-0.0114
	$A_{U3}$	0.0571
	$A_{L0}$	0.1362
	$A_{L1}$	0.2691
	$A_{L2}$	0.1916
	$A_{L3}$	0.1718
	<i>error</i>	$2.3 \times 10^{-4}$

417

418

**Table 5.** Mesh parameters

	Inner domain	Outer domain
Grid type	unstructured	structured
Height	$0.5R$	$2.2R$
Radius	$2.2R$	$4.5R$
Global max element size	0.002	0.003
Max size of layers	$1.2 \times 10^{-4}$	-
Height of layers	$7.5 \times 10^{-6}$	-
Height ratio of layers	1.1	-
Number of layers	5	-

**Table 6.** Parameters of the E387 baseline rotor

<i>Design variable</i>	Lower bound	Upper bound
$A_{U0}^{mid}$	-0.1670	-0.0588
$A_{U1}^{mid}$	-0.1121	0.2246
$A_{U2}^{mid}$	-0.2276	0.1400
$A_{U3}^{mid}$	-0.0808	0.5789
$A_{L0}^{mid}$	0.1231	0.2808
$A_{L1}^{mid}$	0.2119	0.5274
$A_{L2}^{mid}$	-0.0349	0.420

---

$A_{L3}^{mid}$	0.0484	0.7610
$A_{U0}^{tip}$	-0.1670	-0.0588
$A_{U1}^{tip}$	-0.1121	0.2246
$A_{U2}^{tip}$	-0.2276	0.1400
$A_{U3}^{tip}$	-0.0808	0.5789
$A_{L0}^{tip}$	0.1231	0.2808
$A_{L1}^{tip}$	0.2119	0.5274
$A_{L2}^{tip}$	-0.0349	0.4206
$A_{L3}^{tip}$	0.0484	0.7611
$\varphi_{tip} (^{\circ})$	5	20
$\varphi_{mid} (^{\circ})$	15	20
$l_{tip} (mm)$	5	12
$l_{mid} (mm)$	12	20
$d_{mt} (mm)$	30	35
$\varepsilon$	0	0.65

---

425

426

427

428

429

430

431

432 **Table 7.** Optimization formulation

	Function/Variables	Description	Quantity
Minimize	TQ	Rotor torque	1
With respect to		Planform parameters	6
		Airfoil parameters (tip&mid)	16
Subject to	$TH = TH_0$	Rotor Thrust constraint	1
	$\varphi_{mid} > \varphi_{tip}$	Negative twist constraint	1
	$\zeta_U(\psi) > \zeta_L(\psi)$	Airfoil constraint	2
	$t_{max} > 0.045c$	Thickness constraint	2

433

434 **Table 8.** Parameter values of optimization model

Design variable	Value	
	Baseline model	Optimal model
$A_{U0}^{mid}$	-0.0678	-0.05909
$A_{U1}^{mid}$	0.00554	0.1758
$A_{U2}^{mid}$	-0.0114	-0.0279
$A_{U3}^{mid}$	0.0571	0.1501
$A_{L0}^{mid}$	0.1362	0.2783
$A_{L1}^{mid}$	0.2691	0.4054
$A_{L2}^{mid}$	0.1916	0.1730
$A_{L3}^{mid}$	0.1718	0.5448

$A_{U0}^{tip}$	-0.0678	-0.06018
$A_{U1}^{tip}$	0.00554	0.1754
$A_{U2}^{tip}$	-0.0114	-0.01525
$A_{U3}^{tip}$	0.0571	0.3642
$A_{L0}^{tip}$	0.1362	0.2806
$A_{L1}^{tip}$	0.2691	0.5068
$A_{L2}^{tip}$	0.1916	0.2245
$A_{L3}^{tip}$	0.1718	0.3570
$\varphi_{tip} (^{\circ})$	12	7.5381
$\varphi_{mid} (^{\circ})$	25	27.7929
$c_{tip} (mm)$	9	5.1018
$c_{mid} (mm)$	15	12.3889
$d_{mt} (mm)$	33	33.244
$\varepsilon$	0.4	0.3936

435

436 **Table 9.** Data for FSI of baseline model and optimized model

	Baseline model	Optimized model
Element size(mm)	0.5	0.5
Nodes	18814	11737
Max stress (Mpa)	8.232	4.6801
Max deformation(mm)	0.22451	0.25277



Safety factor	6.68	11.75
---------------	------	-------

437

438